JACS
JOURNAL OF THE AMERICAN CHEMICAL SOCIETY

Article

pubs.acs.org/JACS

Oxygen Evolution Reaction Dynamics, Faradaic Charge Efficiency, and the Active Metal Redox States of Ni–Fe Oxide Water Splitting Electrocatalysts

Mikaela Görlin,[†] Petko Chernev,[‡] Jorge Ferreira de Araújo,[†] Tobias Reier,[†] Sören Dresp,[†] Benjamin Paul,[†] Ralph Krähnert,[†] Holger Dau,*[,‡] and Peter Strasser*[,†]

[†]Technical University Berlin, Department of Chemistry, Chemical Engineering Division, Straße des 17. Juni 124, 10623 Berlin, Germany

[‡]Free University of Berlin, Department of Physics, Arnimallee 14, 14195 Berlin, Germany

Supporting Information

ABSTRACT: Mixed Ni–Fe oxides are attractive anode catalysts for efficient water splitting in solar fuels reactors. Because of conflicting past reports, the catalytically active metal redox state of the catalyst has remained under debate. Here, we report an in operando quantitative deconvolution of the charge injected into the nanostructured Ni–Fe oxyhydroxide OER catalysts or into reaction product molecules. To achieve this, we explore the oxygen evolution reaction dynamics and the individual faradaic charge efficiencies using operando differential electrochemical mass spectrometry (DEMS). We further use X-ray absorption spectroscopy (XAS) under OER conditions at the Ni and Fe *K*-edges of the electrocatalysts to evaluate oxidation states and local atomic structure motifs. DEMS and XAS data consistently reveal that up to 75% of the Ni centers increase their oxidation state from +2 to +3, while up to 25% arrive in the +4 state for the NiOOH catalyst under OER catalysis. The Fe centers consistently remain in the +3 state, regardless of potential and composition. For mixed $Ni_{100-x}Fe_x$ catalysts, where x exceeds 9 atomic %, the faradaic efficiency of O_2 sharply increases from ~30% to 90%, suggesting that Ni atoms largely remain in the oxidation state +2 under catalytic conditions. To reconcile the apparent low level of oxidized Ni in mixed Ni–Fe catalysts, we hypothesize that a kinetic competition between the (i) metal oxidation process and the (ii) metal reduction step during O_2 release may account for an insignificant accumulation of detectable high-valent metal states if the reaction rate of process (ii) outweighs that of (i). We conclude that a discussion of the superior catalytic OER activity of Ni–FeOOH electrocatalysts in terms of surface catalysis and redox-inactive metal sites likely represents an oversimplification that fails to capture essential aspects of the synergisms at highly active Ni–Fe sites.

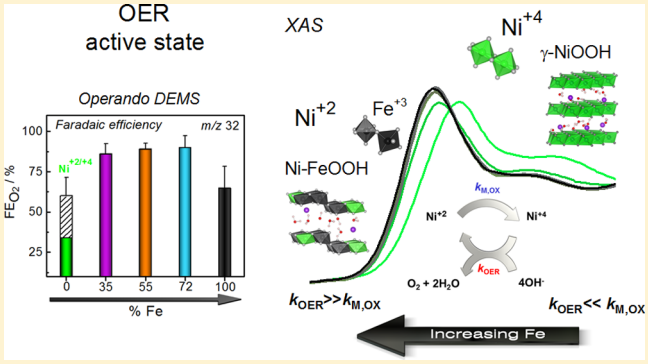

1. INTRODUCTION

The increasing global demand of energy calls for the development of alternative, solar-based energy harvesting technologies, involving integrated photoelectrochemical reactors for efficient solar energy conversion and storage of solar fuels in the form of molecular bonds.[1] To achieve this, earth abundant, nonprecious electrocatalyst materials at anode and cathode are critical. Anode electrocatalysts oxidize water in the oxygen evolution reaction (OER),[2] and cogenerate protons and electrons, while cathode electrocatalysts generate solar fuels.[3−15] Mixed Ni and Fe oxide electrocatalysts are among the most active nonprecious OER catalysts in alkaline electrolyte and help split water at low overpotentials,[16−31] and have been shown applicable to photocatalytic applications.[32−34] Mixed Ni–Fe catalysts containing ~10–50 atomic % Fe have been reported to exhibit most favorable intrinsic OER activities.[30,35−38]

To achieve structural atomic-level and chemical insight into the origin and the mechanism resulting in the low OER overpotential in mixed Ni–Fe electrocatalysts, previous experimental studies have largely relied on the combination of X-ray absorption spectroscopy (XAS), in situ spectroscopic, and voltammetric techniques. Lattice strain, surface area, and conductivity effects have also been brought to the fore; however a common conclusive picture about the metal redox states is still emerging. A missing piece has been the charge transfer reaction dynamics and its selectivity under reaction conditions, in particular in situ deconvolution of the total faradaic charge transfer which goes into forming molecular products vs catalyst charge processes. This contribution will address this issue.

Received: January 11, 2016
Published: March 31, 2016

DOI: 10.1021/jacs.6b00332
J. Am. Chem. Soc. 2016, 138, 5603–5614

Synchrotron-based XAS studies of Ni−Fe catalysts including XANES and EXAFS have repeatedly been used successfully to reveal details on the chemical states and the local atomic structure around the metal centers under catalytic potential. These studies have shown conflicting results regarding the formal charges of the Ni and Fe in the catalytically active state.[18,31,39−44] In situ XAS of a mixed Ni−Fe oxide studied by Landon et al.[18] showed no significant potential-induced changes in local atomic structure or oxidation state under catalytic potential, which was contradicting other studies regarding the oxidation state of Ni atoms during catalysis. The absence of oxidation state changes was attributed to possible electrolyte inaccessible sites which is likely in oxide nanoparticles with a large bulk to surface volume ratio.[18] Operando XAS by Friebel et al.[31] of electrodeposited and/or sputtered Ni-FeOOH electrocatalysts with various compositions of Ni and Fe showed that Ni atoms oxidize from Ni^{2+} to Ni^{4+} during applied potential regardless Ni−Fe composition, with the catalytically active state described as $Ni^{4+}Fe^{3+}OOH$. This in agreement with early EXAFS investigations of Ni-based electrodes by Corrigan and co-workers,[45] which showed that α-$Ni(OH)_2$ converts to γ-NiOOH with Ni in oxidation state +4 under oxidizing potentials. A recent in situ XAS study by Wang et al.[44] of Ni−Fe oxyhydroxide catalysts electrodeposited on carbon paper confirmed Ni atoms in oxidation state +4 and the presence of a highly covalent Fe^{4+}−O bond under OER potential, and a charge transfer between Ni and Fe atoms was proposed. The presence of Fe^{4+} was also proposed in an earlier study by Balasubramanian et al.[41] in electrodeposited Ni−Fe oxyhydroxide catalysts. The presence of Fe^{4+} species under catalytic potentials in a Ni−FeOOH catalyst was recently confirmed by Chen et al.[46] using operando Mössbauer spectroscopy. The role of Fe^{+4} was discussed to potentially provide important mechanistsic implications if generated at an edge, corner, or a "defect" site.[46] Regarding the synergism between Ni and Fe centers, Bates et al.[47] reported a clear difference in the Ni oxidation state in Ni vs Ni−Fe catalysts, where the presence of Fe apparently stabilized Ni centers in a lower oxidation state visible at potentials up to 1.45 V.

In the operando XAS study by Friebel et al.,[31] indications of Fe nucleating as a separate phase was observed above 25% Fe based on diverging Fe−O and Ni−O distances, which could explain why the OER activity did not improve above this Fe content. Moreover, Trotochaud et al.[28] showed that traces of Fe impurities in the electrolyte readily incorporate into the Ni oxyhydroxide lattice, which increases the OER activity of α-NiOOH due to the presence of Fe and not due to formation of β-NiOOH which was long proposed as the reason for increased activities of NiOOH catalysts after aging in KOH. Klaus et al.[48] showed that despite removal of Fe impurities, mixed phases of α, β, and γ phases in Ni oxyhydroxides are likely to form; however, Fe impurities resulted in a lower degree of β-$Ni(OH)_2$ formation upon aging based on in situ spectroscopic Raman measurements. Using DFT calculations, Friebel et al.[31] showed that OER intermediates have nearly optimal binding energy at Fe sites located in proximity to a Ni site,[31] thus Fe was proposed as the expected active site. Trześniewski et al.[42] observed negatively charged species referred to as "active oxygen" in Ni(Fe)OOH in KOH pH 13 using Raman spectroscopy, which was absent in borate buffer pH 9.2, explaining the strong pH dependence of OER catalysis.

Direct comparison between studies is notoriously demanding due to deviating experimental parameters, catalyst supports, or other variations in electrochemical testing conditions. Despite these difficulties, recurring OER activity trends and structural motifs have been observed in systematic studies across, which are necessary to eventually lend support to the yet incomplete mechanistic picture of the catalytic interface processes.

In this contribution, we provide new insight into the Ni−Fe OER puzzle by combining operando differential electrochemical mass spectrometry (DEMS), quasi-in situ X-ray absorption spectroscopy (XAS)[49,50] and electrochemical characterization. The DEMS analysis yields reaction product dynamics data that allowed for a quantitative deconvolution of faradaic charge generating molecular oxygen and charge injected into the metal oxide catalyst causing redox state changes. This constitutes a first-of-its-kind cross-check of our XAS-based findings on the metal redox states. A simple but plausible hypothesis is brought forward to reconcile our and previous findings with respect to the redox states of the metal centers under catalytic oxygen evolution conditions.

2. EXPERIMENTAL SECTION

2.1. Synthesis of Mixed Ni−Fe Catalysts. Nanosized Ni−Fe catalysts with varying Ni/Fe ratios were synthesized by a microwave-assisted, surfactant-free solvothermal route.[51,52] This allowed for high solubility of the Fe^{3+} precursor under these conditions. Desired amounts of solutions of 0.1 M $Ni(NO_3)_2{\cdot}6H_2O$ (99.999% trace metals basis, Aldrich) and 0.1 M $Fe(acac)_3$ (99.5% trace metal basis, Aldrich) with additions of 10 mM 1,2-Benzenediol (>99%, Aldrich) were mixed in benzyl alcohol (Puriss, 99−100.5%) to make up a final total concentration of 22 mM of Ni+Fe precursors to a volume of 20 mL. The reaction mixtures were sealed in special autoclave vials (Anton Paar) and heated to 190 °C for 15 min with a ramping step of 16.5 °C/min. After immediate cooling to room temperature the solid products were collected by washing five times with high purity ethanol and recollected by repetitive centrifugation at 7500 rpm for 15 min. The collected nanoparticles were freeze-dried and stored as powders under inert atmosphere until use. An Fe-free Ni-catalyst was prepared according to the same synthesis method but with an additional purification step where the solvent and the ethanol had been cleared of Fe-traces prior to synthesis according to the method reported by Trotochaud et al.[28] An additional Fe-Free Ni-catalyst was synthesized without addition of 1,2-Benzenediol using the same conditions.

2.2. Elemental Analysis. The metal content was determined by inductively coupled plasma−optical emission spectrometry (ICP-OES), using a Varian 715-ES spectrometer with a CCD detector. Prior to analysis, the samples were digested in mixtures of concentrated HNO_3:HCl in a 1:3 ratio for ∼2 h and sonicated for 10 min and diluted with appropriate amounts of >20 MΩ cm Milli-Q water.

Total metal content in catalysts after electrochemical conditioning was analyzed using total reflection X-ray fluorescence (TXRF) spectroscopy. Conditioned electrodes were dissolved in 300 μL of HCl (37%, Merck) by sonication for ∼10 min, and further left in the HCl solutions for at least 2 h. Additions of the same amount of a Ga-standard solution of 1 mg/mL (Merck), allowed for determination of the metal content. The analysis was acquired using a PicoTAX spectrometer with a 40 kV using a Si-drift detector (Röntec).

2.3. Scanning Electron Microscopy (SEM) and Energy Dispersive X-ray (EDX) Analysis. SEM images of samples drop-casted on polished glassy carbon electrodes were acquired in secondary electron mode using a JEOL JSM-7401F high resolution field emission SEM operated at 10 kV or, respectively, 15 kV, if the images were acquired in the context of energy dispersive X-ray (EDX) spectroscopic measurements. EDX analysis (including elemental mapping and line-scans) was measured in the same microscope using an EDX detector unit (Quantax 400, BrukerAXS Microanalysis GmbH, Germany). The working distance was 12 mm for EDX elemental mapping and line-scan analysis. Quantifications of the Ni and Fe content were obtained from the *K* lines.

DOI: 10.1021/jacs.6b00332
J. Am. Chem. Soc. 2016, 138, 5603−5614

2.4. Powder X-ray Diffraction (XRD). XRD was recorded using a Bruker D8 advance powder diffractometer (Bragg−Brentano geometry), equipped with a Cu Kα source, variable divergence slit and position sensitive device as detector. Data were recorded between 10° to 80° 2θ with a step size of 0.038°.

2.5. Electrochemical Characterization. The catalytic activity was measured in rotating disk electrode setup (RDE) using a standard 3-electrode electrochemical cell designed to hold the glassy carbon electrode (Φ = 5 mm), a Pt-mesh counter electrode, and a reversible hydrogen reference electrode (RHE). The electrodes were polished with 2 μm followed by 0.05 μm silica polishing solutions (Buehler), and sequentially washed with Milli-Q - 2-Propanol - Milli-Q water in a sonication bath. Trace metals were removed with HCl and the washing procedure repeated. All measurements were recorded in 0.1 M KOH (semiconductor grade, 99.99% trace metals basis, Aldrich) in electrolyte purged with N_2 for 20 min prior to the experiments (and keeping a protective N_2 atmosphere), using a GAMRY potentiostat 3000 at a rotation speed of 1600 rpm. Catalyst powders were prepared as inks with mixtures of 50:75:1 of Milli-Q water, 2-propanol, and 5 wt % Nafion (SIGMA). The inks were homogeneously dispersed by ultrasonication for ∼20 min, and drop-casted onto the glassy carbon electrodes to make up a total metal loading of ∼5 μg of Ni+Fe cm^{-2} (∼175 nmol of Ni+Fe cm^{-2}), and dried in an oven at 60 °C for 10 min. Fe-free KOH was prepared by purification according to a reported method,[28] measured in polypropylene beakers (Nalgene) instead of the standard electrochemical cell to avoid contamination from glass etching. The uncompensated series resistance (*iR*-drop) was determined by electrochemical impedance spectroscopy (EIS) in the frequency range between 1 Hz to 100 kHz, with typical values in 0.1 M KOH of 30 Ω. CVs were corrected afterward for *iR*-drop whereas chronoamperometric measurements were carried out at *iR* compensated potentials determined prior to the measurement.

2.5.1. Turnover Frequency (TOF) and Ni Redox Charge Calculations. The turnover frequency was defined as moles of O_2 per moles of total metal content (Ni+Fe) evolved per second (s^{-1}). The geometric current densities (i) were extracted at 300 mV overpotential (1.53 V_{RHE}, all reported potentials are *iR* corrected) and 400 mV overpotential (1.63 V_{RHE}) from quasi stationary state measurements, based on the total moles of Ni+Fe (n_{Ni+Fe}) on the electrode determined by ICP-OES prior to the measurement, assuming a z = 4 electron transfer for the overall reaction according to eq 1,

$$\mathrm{TOF} = \frac{i}{z \cdot F \cdot n_{\mathrm{Ni+Fe}}} \tag{1}$$

Determination of redox charge (Q) (equivalent to the number of redox active Ni atoms) was done by integration of the area under the voltammetric prewave ascribed to the $Ni(OH)_2$/NiOOH redox transition. The redox charge was described as the area between the experimental curve and a fit line described by the Butler−Volmer equation, $i_a = i_0^{(1-\alpha)F\eta/RT}$. The fit was minimized by the nonlinear least-squares method using the Levenberg−Marquardt algorithm using in-house software. To obtain the redox number (electrons transferred per Ni atoms, e^- Ni^{-1}), the integrated charge was normalized to the total moles of Ni on the electrode determined by ICP-OES prior to, or by TXRF analysis after electrochemical conditioning, according to eq 2,

$$e^- \text{ per Ni} = \frac{Q_{\mathrm{Ni(OH)_2/NiOOH}}}{z \cdot F \cdot n_{Ni}} \tag{2}$$

2.6. Differential Electrochemical Mass Spectrometry. Differential electrochemical mass spectrometry (DEMS) was recorded in a home customized dual thin-layer electrochemical flow cell based on the concept reported elsewhere.[53] The volatile products were detected using a Prisma quadrupole mass spectrometer (QMS 200, Pfeiffer-Vacuum) equipped with two turbomolecular pumps (HiPace 80) operating under 10^{-6} mbar.

The electrolyte was separated from the chamber by a hydrophobic PTFE membrane with a pore size of 30 nm and thickness of 150 μm (Cobetter, Cat. No. PF-003HS). The catalysts were drop-casted on polished glassy carbon electrodes (Φ = 5 mm, HTW GmbH) as described in section 2.5, to make up a total metal loading of ∼10 μg Ni +Fe cm^{-2} determined by ICP-OES. Cyclic voltammograms (CVs) were recorded in 0.1 M KOH by cycling the potential between 1.0−1.8 V_{RHE} (prior to *iR*-compensation) at a scan-rate of 50 mV/s. The electrodes were initially allowed to stabilize in electrolyte solution at 1.1 V_{RHE}, in order to record the ionic current baseline before recording the CVs. The electrolyte was constantly purged with N_2 before entering the flow cell and pumped through the cell at a flow of 8 μL/s. Formation of volatile products (m/z 2, 16, 18, 28, 30, 36, 32, 34, 44) was monitored during the CV scan. Quantification of the Faradaic efficiency (FE) of O_2 (m/z 32) was done using a calibration constant (K^*) obtained from quasi-stationary state measurements where chronoapotentiometric steps were applied in the linear region. The value of K_j^* directly relates the mass spectrometric ion current (i_{MS}) to the faradaic current at the potentiostat (i_F) to the volatile product j according to eq 3,[54]

$$K_j^* = \frac{i_{\mathrm{MS},j} \cdot z_j}{i_F} \tag{3}$$

where z_j represents the number of transferred electrons per molecule of volatile product j. The Faradaic efficiency (charge selectivity) during a CV scan was obtained by integration of the mass spectrometric ion current ($Q_{\mathrm{MS},j}$) and the capacitive current-corrected, faradaic current (Q_F), and combining the two integrated charge values according to eq 4,[55]

$$\mathrm{FE}\ (\%) = \frac{Q_{\mathrm{MS},j} \cdot z_j}{Q_F \cdot K_j^*} \cdot 100 = \frac{Q_{F,j}^{\mathrm{DEMS}}}{Q_F} \cdot 100 \tag{4}$$

Here $Q_{F,j}^{DEMS}$ denotes the DEMS-derived, total faradaic charge that is converted into volatile product j. Only anodic faradaic currents were included in the analysis to exclusively account for anodic processes (molecular O_2). The potential/time integration limits of the mass currents were selected from the onset of O_2 formation (m/z 32) until the detected signal had returned to the initial baseline level. The absolute integration limits slightly varied for different Ni:Fe compositions due to different onset potentials for OER.

2.7. X-ray Absorption Spectroscopy (XAS). X-ray absorption spectra were recorded at the K-edges of Ni and Fe at the KMC-1 and KMC-3 beamlines at the BESSY-II synchrotron facility at Helmholtz-Zentrum Berlin, Germany, using a liquid-helium cryostat cooled to 20 K.[56] Absorption spectra were collected in fluorescence mode of films conditioned at OER potentials and in absorption and fluorescence mode of as-prepared powder samples. The fluorescence was detected using a 13-element energy-resolving Ge detector (Canberra), selecting the K_α emission lines of the respective element. The k^3 weighted extended X-ray absorption fine structure (EXAFS) spectra were extracted using E_0 value equal to 8333 eV at the Ni K-edge and to 7117 eV at the Fe K-edge. Theoretical simulations of the EXAFS spectra were carried out using in-house software (SimX) with phase functions generated from the atomic coordinates of α-$Ni(OH)_2$, γ-NiOOH, γ-FeOOH, and α-FeOOH, using the FEFF software package[57,58] version 9.1 with self-consistent field option switched on. The amplitude reduction factor (S_0^2) was set to 0.85 for both Ni and Fe K-edges. The data ranges used for the simulations were 25−750 eV above E_0 (k-range of 2.6−14 $Å^{-1}$) for the Ni K-edge and 25−600 eV (2.6−12.5 $Å^{-1}$) for the Fe K-edge. The simulations were optimized in k-space by the least-squares method using a Levenberg−Marquardt algorithm with numerical derivatives. The error ranges of the fit parameters were estimated from the covariance matrix of the fits corresponding to a 68% confidence level as described elsewhere.[49] More details about selected fit parameters are given in Supporting Information S6.

2.7.1. Sample Preparation for Quasi-In Situ XAS. Catalyst inks were prepared as described above without additions of Nafion, and drop-casted on polished glassy carbon working electrodes with a geometric area of ∼1 cm^2, and prepared for quasi-in situ XAS as described previously.[49,50] Catalysts were assembled in custom-made

DOI: 10.1021/jacs.6b00332
J. Am. Chem. Soc. 2016, 138, 5603−5614

sample holders designed to hold a small volume of electrolyte on top of the working electrode. A Pt-wire was used as counter electrode and an RHE reference electrode connected to the working electrode via a Luggin capillary to the electrolyte. The *iR*-drop was determined by EIS prior to the measurement, which showed typical values of 2 Ω. Oxygen evolution potential was applied using a GAMRY 3000 potentiostat and the catalysts were conditioned at 1.0 or 1.63 V_{RHE} for 30 min in 0.1 M KOH (semiconductor grade, 99.99% trace metals basis, Aldrich) without further purification. The catalysts were freeze quenched in liquid N_2 during applied potential. All samples were stored in liquid N_2 until analyzed at the BESSY-II synchrotron facility, Helmholtz-Zentrum, Berlin.

3. RESULTS AND DISCUSSION

3.1. Electrochemical Activity, Turnover Frequency, Voltammetric Metal Redox Behavior. Mixed Ni−Fe oxyhydroxide catalysts with atomic compositions ranging from 0 to 100 at % Fe were prepared using solvothermal synthesis. Consistent with earlier reports they showed high catalytic activity for the oxygen evolution reaction (OER) in a specific compositional range. The highest oxygen evolution activity was observed for the $Ni_{45}Fe_{55}$ catalyst containing 55 at. % Fe (Figure 1a,b and S1a−c), demonstrating a synergism between Ni and Fe centers in accordance with previous studies.[18,19,24,37,59−61] The lower limits of the catalytic turnover

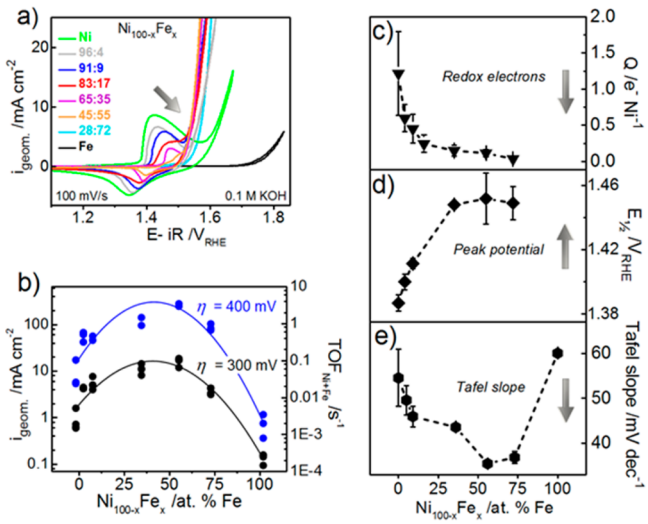

Figure 1. Electrochemical characterization of mixed Ni−Fe catalysts with varying catalyst composition ($Ni_{100-x}Fe_x$) measured in RDE setup in 0.1 M KOH. (a) Cyclic voltammograms (CVs) recorded at a scan-rate of 100 mV/s after conditioning at 1.63 V_{RHE} for 30 min (see also Figure S1a for CVs at 10 mV/s). (b) Geometric current density ($i_{geom.}$) and turnover frequency (TOF) of Ni−Fe catalysts based on the total metal loading of Ni+Fe (chosen identical for all samples) extracted from stationary measurements at η_{OER} = 300 mV (black curve) and 400 mV (blue curve). TOF is defined as moles of O_2 evolved per total moles of metal (Ni+Fe) per second. (c) Number of electrons transferred per Ni atoms (e^- Ni^{-1}) obtained by integration of the area under the $Ni(OH)_2$/NiOOH redox peak obtained by integration of the area under the redox peak, obtained from the maximum average value of anodic and cathodic redox wave during the first 150 cycles, $\left(\frac{Q_{p,a}+Q_{p,c}}{2}\right)$ (d) Midpeak potential, $\left(\frac{E_{p,a}+E_{p,c}}{2}\right)$ of the $Ni(OH)_2$/NiOOH redox peak. (e) Tafel slopes obtained from quasi-stationary state measurements (see also Figure S1d). Catalyst loadings were determined by ICP-OES analysis. Additional electrochemical measurements are presented in Supporting Information S1.

frequency based on total metal of Ni + Fe determined by ICP-OES (TOF_{Ni+Fe}) at η = 300 mV was determined to 0.14 s^{-1} for the $Ni_{45}Fe_{55}$ catalyst in 0.1 M KOH (Figure 1b, see also Figure S1c for mass based activity). The upper limit TOF, based on the redox active Ni centers obtained by integration of the $Ni(OH)_2$/NiOOH redox peak area of the $Ni_{45}Fe_{55}$ catalyst under the same conditions was estimated to 2 s^{-1}. Direct comparison to other work is rather challenging due to variations in a number of parameters such as catalyst loading[62,63] and electrochemical conditions as well as the definition of the active site, the approach to evaluate redox active sites, and the contribution of these to the overall activity.[15,61] The values we observe meet or exceed previous estimations of likely catalytic turnover frequencies of mixed Ni−Fe catalysts.[19,30,61,64] The redox electrons (e^- per Ni atoms) of the $Ni(OH)_2$/NiOOH redox transition visible in the CVs at ∼1.4 V_{RHE} was estimated to ∼1.1 for the Ni-catalyst on the anodic scan, and slightly higher on the cathodic scan (Figure 1c), well consistent with previous reports on NiOOH catalysts.[19,59] In other words, every metal center in our Ni-catalyst appear to undergo an oxidation state change assuming 1 electron transfer. Upon addition of Fe, however, this number is substantially decreased, with an associated anodic peak shift of ∼70 mV when the Fe content is increased from 0 to 50% Fe (Figure 1d). Addition of Fe also had an evident effect on the Tafel slopes, which varied between 35 mV dec^{-1} for the most active $Ni_{45}Fe_{55}$ catalyst to 60 mV dec^{-1} for less active catalysts (Figure 1e and S1d).

Addition of small traces of Fe (4%) resulted in a drastic decrease of the redox electrons to 0.5 e^- per Ni, with a further decrease down to ∼0.1 for the $Ni_{45}Fe_{55}$ catalyst. This effect was previously noted for electrodeposited Ni−Fe catalysts by Louie et al.,[30] which was referred to as a decrease in the average oxidation state of Ni. Stabilization of the Ni in lower valent states in a mixed Ni−Fe catalyst on Raney-nickel support was observed by Bates et al.,[47] however at relatively low overpotentials (1.45 V). In a study by Friebel et al.,[31] Fe incorporation in mixed Ni−Fe oxyhydroxides did not appear to have any effect on the formal oxidation state of Ni. The origin of this discrepancy has not yet been clearly elucidated.

To eliminate the possibility of trapped oxidized Ni^{4+} escaping detection due to formation of an insulating layer of non-conductive $Ni^{2+}(OH)_2$ at the electrode interface as was recently discussed by Batchellor et al.,[62] catalysts were investigated before and after application of a reducing potential of 0 V_{RHE} for 20 min. We found, in accordance with the study,[62] that the redox wave in the first CV when starting in the "reduced state" appeared larger than in the steady state CVs, without significant changes in the cathodic redox wave (Figure S2). The increase in the anodic wave was clearly dependent on the Ni:Fe stoichiometry, where largest effect was observed for the $Ni_{91}Fe_9$ catalyst, similar to the composition where a large change was demonstrated by Batchellor et al.[62] Increased catalyst loading has also been shown to result in increased OER activity.[62,63] Starting in the "reduced state" did not result in an instant increase in the OER activity on the anodic scan for any of the Ni−Fe catalysts, where a larger fraction of Ni centers hypothetically should be exposed to the electrolyte as suggested by the increased redox wave, and thus a direct correlation between the observed effect and increased electrolyte accessibility is not strongly supported by these observations. Other possibilities include processes related to adsorption intermediates or formation of low valent $[Ni^{+2}-OOH]^-$

DOI: 10.1021/jacs.6b00332
J. Am. Chem. Soc. 2016, 138, 5603−5614

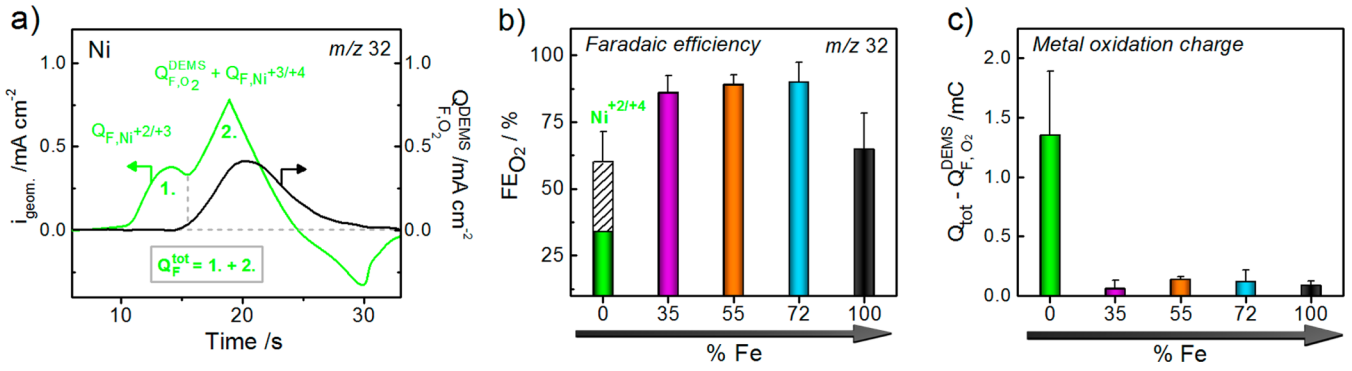

Figure 2. Operando DEMS during CVs in the OER region between 1 and 1.8 V_{RHE} (before *iR*-comp.) in 0.1 M KOH (a) In situ cyclic voltammetric scan (green curve) and the corresponding faradaic ion current of O_2 (m/z 32) (black curve) of the Ni-catalyst. Q_F^{tot} represents the total anodic charge under the green trace, and $Q_{F,O2}^{DEMS}$ is derived from the charge under the black ion current trace. (b) Faradaic O_2 efficiencies of Ni−Fe oxyhydroxide catalysts as a function of Fe-content ($Ni_{100-x}Fe_x$) given as atomic %. The hatched bar represent the O_2 efficiency excluding the charge associated with $Q_{F,Ni+2/+3}$, corresponding to the $Ni(OH)_2$/NiOOH redox process. The Faradaic O_2 efficiency was derived from FE_{O2} (%) = $Q_{F,O2}^{DEMS}$/Q_F^{tot}. (c) Absolute faradaic charge (Q_F^{tot} − $Q_{F,O2}^{DEMS}$) injected into catalyst layer for changing metal oxidation states. The catalyst composition ($Ni_{100-x}Fe_x$) is given as atomic % Fe on x-axis. The catalyst loading was ∼10 μg/cm^2. Error bars are derived as the standard deviation from 3 independent measurements. Additional measurements are presented in Supporting Information S2 (Figure S7−S9).

species during the first CV scan as was recently discussed by Smith et al.[65]

Conditioning of the catalysts by CV cycling or, alternatively, application of a constant electrode potential of +1.63 V showed distinct changes in the OER activity (Figure S3) associated with a change in the number of redox electrons transferred during the first 150 cycles (Figure S4a,b) accompanied by an anodic peak shift of ∼30 mV (Figure S4c,d). These changes could be either a consequence of hydration, loss of catalyst,[13,63] or continuous Fe incorporation.[28] To address possible losses of catalyst, comparison of metal content of as-prepared catalysts and after the conditioning step determined by TXRF analysis, showed a loss of ∼30% total metal , which was similar for both the Ni and Ni−Fe catalysts, thus suggesting that the e^- per Ni was slightly underestimated (see Figure S5 for reviewed redox electrons). There was also a loss of Ni (not only Fe) during this conditioning step; however, the relative loss of Fe was consistently higher under these conditions resulting in a small, however neglectible fractional change (∼6%). A stable CV was achieved after the conditioning step upon further cycling, suggesting that these initial losses could be due to stress under strong oxygen evolution conditions.

Experiments of the Ni-catalyst were repeated in Fe-free electrolyte purified according to the method by Trotochaud et al.[28] These experiments showed that elimination of Fe impurities from the KOH electrolyte (case 3 in Figure S6a) increased the OER overpotentials at 10 mA cm^{-2} by about 180 mV compared to the unpurified or Fe-Free KOH conditions (cases 1,2), in agreement with previous observations upon removal of Fe-impurities.[48] An additional redox peak appeared at 1.56 V_{RHE} (Figure S6a). The relative activity and Ni redox peak charge evolution during the first 150 cycles under Fe-Free conditions exhibited similar trends as the Ni-catalyst measured in unpurified electrolyte; however, under Fe-free conditions the OER activity was descending (Figure S6b,c). Since a proper method was lacking to determine whether Fe-impurities still remained in the catalysts, we cannot claim that trace Fe-impurities did not affect the measured curves. It is on the other hand likely that processes such as phase transformations and coexistence of α, β and γ phases occur even under Fe-Free conditions, recently demonstrated by Klaus et al.[48]

The reaction dynamics analysis has evidenced that application of oxidizing potentials results in pronounced and complex changes in redox properties and catalytic activity extending over a time period of 10 min (maximal OER activity) up to 30 min (approximate equilibration reached). The origin of these changes may be related to trace Fe impurities; however, a partial influence by a loss of catalyst material (∼30%) was confirmed. As a conclusion, our analysis shows that the extent of redox-state changes detected in Ni-containing catalysts implies that not only surface exposed metal sites are redox-active, but that a catalytic volume activity of the catalyst material is more likely as previously found for amorphous oxides.[66,67]

3.2. Faradaic Charge Efficiency Derived from In Situ Differential Electrochemical Mass Spectrometry (DEMS).

To learn more about the reaction dynamics of the OER process, volatile product species were detected under catalytic conditions using operando differential electrochemical mass spectrometry (DEMS). The operando DEMS analysis allowed for a separation of the total faradaic anodic charge, Q_F^{tot}, transferred during a cyclic voltammetric OER scan, into two components: (1) the faradic charge $Q_{F,O2}^{DEMS}$, which corresponds to the number of oxidizing equivalents consumed for water oxidation (O_2 formation), (2) the oxidation charge, $Q_{F,M}$, which corresponds to the number of redox-equivalents needed for oxidation-state changes of the metal centers.

The voltammetric profiles obtained in the DEMS setup were nearly identical to those previously measured using the RDE setup (see Figure 1a and Figure S7−S8). This lent support to the accuracy of our DEMS-based faradaic charge analysis. No volatile products other than molecular O_2 (e.g., no CO_2) were detected during anodic polarization of the Ni−Fe oxyhydroxide electrocatalysts over the entire compositional range. Figure 2a exemplifies our analysis for the Ni catalyst. The anodic charge under the voltammetric curve (green) represents the total faradaic charge Q_F^{tot}. The charge under the mass spectrometric trace (black) is $Q_{MS,O2}$ which can be converted into $Q_{F,O2}^{DEMS}$. The quantity Q_F^{tot} splits into a component associated with oxidation of Ni centers, $Q_{F,Ni}$, and a component associated with the evolution of O_2, $Q_{F,O2}^{DEMS}$.

DOI: 10.1021/jacs.6b00332
J. Am. Chem. Soc. 2016, 138, 5603−5614

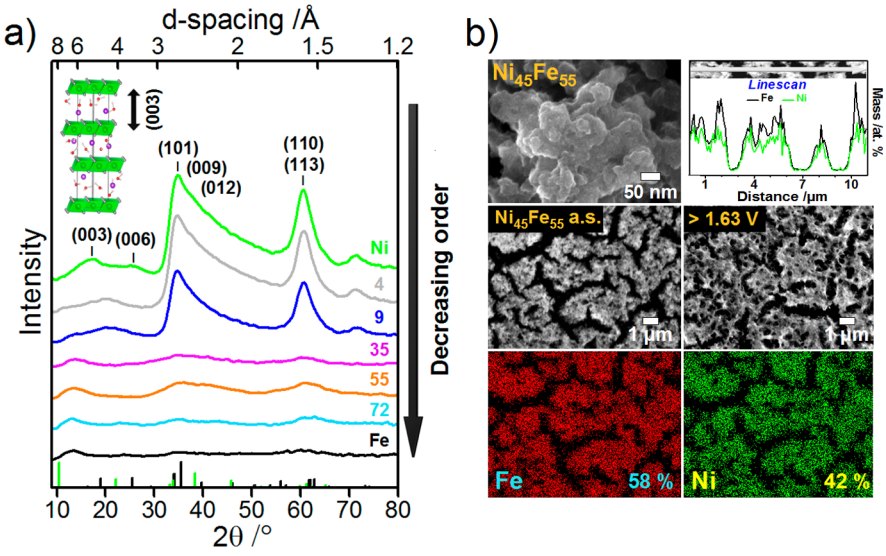

Figure 3. (a) Powder XRD diffractograms of as-prepared Ni–Fe(OOH) catalysts with varying Ni:Fe compositions ($Ni_{100-x}Fe_x$). The inset shows the structural motif of α-$Ni(OH)_2$ with the arrow indicating the (003) interlayer spacing. The Fe content is indicated as atomic % Fe determined by ICP-OES. The bottom green vertical lines show the diffraction peaks of α-$Ni(OH)_2$ (pdf # 00–038–0715) and of FeOOH (0015441[75]). (b) SEM image (top left and middle) and EDX elemental mapping (bottom) of the $Ni_{45}Fe_{55}$ catalyst; as-prepared catalyst. A line-scan analysis with the relative change of the Ni and Fe content across a selected path of the as-prepared catalyst is shown in the upper right corner. Atomic compositions are reported as atomic %. See also Figure S12–13 for additional SEM-EDX elemental mapping after exposure to OER catalytic conditions.

For the Ni-catalyst, the experimental faradaic efficiency of the O_2 evolution process, FE_{O2}, can be evaluated according to eq 5,

$$FE_{O2} = Q_{F,O2}^{DEMS}/Q_F^{tot} = Q_{F,O2}^{DEMS}/(Q_{F,O2}^{DEMS} + Q_{F,Ni}) \quad (5)$$

was about 33%, (see green bar in Figure 2b). We note that this value of FE_{O2} was almost identical in nonpurified (Fe-containing) electrolyte and in Fe-free electrolyte. Given the absence of any other volatile product, this result implies that 67% of Q_F^{tot} constitutes faradaic charge solely used to change the oxidation state of Ni atoms. If the 1-electron $Ni^{2+/3+}$ redox charge process (see peak area "1." in Figure 2a) was subtracted from Q_F^{tot}, the resulting FE_{O2} value roughly doubled to 60% (hatched bar in Figure 2b). This still leaves a significant portion of the experimental anodic charge unaccounted for.

To account for this missing charge, we assume that $Q_{F,Ni}$, splits into $Q_{F,Ni+2/+3}$, the contribution from the 1-electron $Ni^{2+/3+}$ transition, and into $Q_{F,Ni+3/+4}$, associated with the consecutive 1-electron redox transition from Ni^{3+} to Ni^{4+}, according to eq 6,

$$Q_{F,Ni} = Q_{F,Ni+2/+3} + Q_{F,Ni+3/+4}. \quad (6)$$

Eq 6 is a plausible assumption given the much more anodic electrode potentials during the OER compared to the $Ni(OH)_2$/NiOOH redox peak potential (Figure 1a). Simple algebra yields eq 7,

$$Q_{F,Ni+3/+4} = 0.25 \times Q_{F,Ni+2/+3} \quad (7)$$

for the data of the Ni-catalyst (see derivation eqs S1–S5).

Considering our earlier conclusion that all Ni centers of the Ni-catalyst reached the Ni^{3+} oxidation state, our DEMS-based charge balance analysis in eq 5 clearly evidence the formation of Ni^{4+}; in particular a maximum of 25% of all Ni centers had reached the Ni^{4+} state during the scanned OER conditions. Figure 2c highlights the absolute charge ($Q_F^{tot} - Q_{F,O2}^{DEMS}$) that was injected into the Ni redox state changes for the Ni-catalyst. Figure 2b suggests that the faradaic contribution of the evolved O_2 (m/z 32) differed substantially at higher Fe contents. The O_2 faradaic efficiency reached a maximum at intermediate Ni:Fe compositions (35, 55, and 72% Fe) before it dropped again for the pure Fe catalyst. This was quite similar to the OER activity trends discussed before.

For the mixed Ni–Fe oxide catalysts, an evaluation of $Q_{F,Ni+2/+3}$ is no longer possible, because the anodic redox feature vanished or shifted anodically merging with the OER voltammetric profile. The much larger FE_{O2} values of the $Ni_{65}Fe_{35}$, $Ni_{45}Fe_{55}$ and $Ni_{28}Fe_{72}$ catalysts (Figure 2b) evidenced less metal redox charge processes relative to oxygen evolution charge. Thus, the average Ni valence in the mixed Ni–Fe catalysts must have remained lower compared to the Ni-catalyst. In fact, Figure 2c confirms how much the metal redox charge dropped in the presence of Fe. Fe appears to have a stabilizing effect on low-valent Ni centers, which largely suppresses the oxidation of Ni to higher oxidation states under OER conditions. This will be further complemented with X-ray absorption studies below.

Unlike the Ni-catalyst, the Fe catalyst showed little charge contribution toward oxidation state changes (Figure 2c) suggesting that Fe centers largely remained in their oxidation state even at catalytically active OER electrode potentials. The somewhat lower FE_{O2} value directly reflects the lower catalytic OER rate compared to the mixed Ni–Fe catalysts, which lowers the relative contribution of $Q_{F,O2}^{DEMS}$. Additional measurements were carried out with extended scan-limits in order to reach a similar O_2-rate for all Ni–Fe catalysts (Figure S7f,g and S8f,g). These measurements confirmed a higher FE_{O2} value of the Fe catalyst when cycling to higher current densities (Figure S9). However, at such high overpotentials, other processes such as catalyst degradation and carbon corrosion might lower the overall efficiency.

In summary, our DEMS-based faradaic efficiency analysis provided independent evidence for a $Ni^{2+/4+}$ transition for the Ni-catalyst under OER conditions. In contrast, the presence of

DOI: 10.1021/jacs.6b00332
J. Am. Chem. Soc. 2016, 138, 5603–5614

Fe caused much higher faradaic efficiency, FE_{O2}, with values of ~90% for the most active mixed Ni–Fe catalysts. This evidence highly O_2-selective catalytic OER cycles, while Fe appears to reduce the detectable amounts of high-valent Ni.

3.3. Compositional Analysis, Long-Range Order and SEM-EDX Elemental Mapping. X-ray diffraction of the mixed Ni–Fe catalysts (Figure 3a and Figure S10) showed broad diffraction peaks at 15° and 25°, corresponding to the (0 0 3) and (0 0 6) lattice planes associated with the interlayer spacing of the layered $Ni(OH)_2$.[68] Broad diffraction peaks were also visible at ~40° and 61° 2θ; the peak at 40° could be refined with three peaks at 35°, 38°, and 45°. These all match well with observations of turbostratic α-$Ni(OH)_2$.[28,68–73] The Fe catalyst showed reflections at similar positions, 14°, 20°, 36°, and 60° 2θ, however with lower intensity, which have been reported for highly distorted FeOOH structures.[74–79] The *d*-spacings were found between ~6–8 Å obtained from the (0 0 3) reflection, with small variations as a function of Fe-content. Changes in turbostratic oxyhydroxide structures are difficult to accurately interpret due to *c*-axis stacking faults.[24,28,40,73,80–82] The relative peak intensities of the (1 0 1) and (1 1 0) reflections continued to decrease at increased Fe content, which is consistent with formation of more distorted phase, in line with earlier observations of the effect of Fe intrusion in Ni lattices.[30,36]

Scanning electron micrographs (SEM) of the Ni and the $Ni_{45}Fe_{55}$ catalysts showed a similar layered morphology with stacked, slightly distorted layers with a layer size of ~100 nm (see Figure 3b and Figure S11a–c). The morphology of the Fe catalyst revealed a much smaller domain size with small particles <10 nm, which partly assembled to form larger round agglomerated particles in the size of ~500 nm (see Figure S11d–f). This would suggest that the low XRD amplitudes observed for the Fe catalyst could have been influenced by the small particle size. The Ni-catalyst before and after exposure to catalytic potentials (1.63 V for 30 min in 0.1 M KOH) did not show detectable amounts of Fe impurities; however, traces of Fe could be below the detection limits. Elemental EDX mapping and line-scan analysis of the $Ni_{45}Fe_{55}$ catalyst showed a homogeneous distribution of Ni and Fe across the analyzed area (Figure 3b and Figures S12–S13), with a significant amount of oxygen distributed in the metal associated regions both of the as-prepared catalyst and after conditioning at catalytic OER potential. The EDX analysis indicated a relative loss of Fe content, resulting in a fractional change of ~9% after OER catalysis (see Figure 3b and Figure S12), which was also confirmed by TXRF analysis as a ~6% loss (see discussion above). Apparent changes were also visible in the morphology after exposure to 1.0 and 1.63 V (Figure S13). The EDX mapping showed that Ni and Fe remained well distributed without visible formation of separate phases.

3.4. Quasi-In Situ X-ray Absorption Spectroscopy (XAS). Gaining access into prevalent local structural motifs, atomic coordination number and bond lengths of the mixed Ni–Fe catalysts was achieved using X-ray absorption spectroscopy (XAS) at the Ni and Fe *K*-edges. Catalysts with different compositions of Ni and Fe were drop-casted onto glassy carbon electrodes at a geometric metal loading of ~145 nmol/cm^2. Catalytic voltages of ~1.63 V_{RHE} (η_{OER} = 400 mV) were applied during 30 min in 0.1 M KOH as the conditioning step. The catalysts were freeze-quenched under applied potential using liquid N_2 according to a previously reported approach.[66,83] Selected catalysts were also investigated under non catalytic potentials of 1.0 V_{RHE}.

3.4.1. Local Structure and Metal Redox States. X-ray absorption near-edge structure (XANES) showed that the Fe centers were consistently in oxidation state +3 both in as-prepared catalysts and catalysts freeze-quenched in the OER-active state (Figure 4a and Figure S14a), which have been

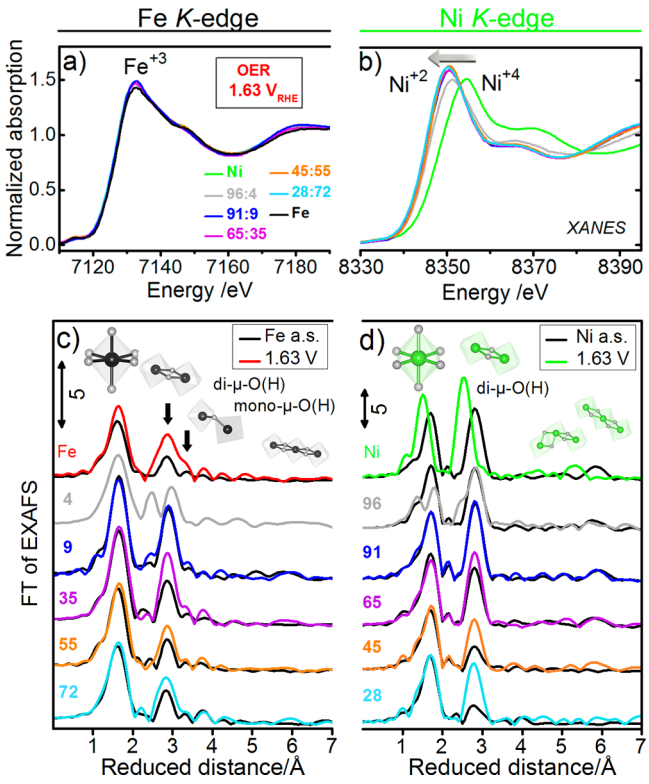

Figure 4. X-ray absorption spectra of the Ni–Fe catalysts with varying catalyst composition ($Ni_{100-x}Fe_x$) freeze-quenched under application of catalytic potential after conditioning at 1.63 V for 30 min in 0.1 M KOH. (a) Fe *K*-edges and (b) Ni *K*-edges. Fourier transformed k^3-weighted EXAFS oscillations (FT-EXAFS) of as-prepared (a.s.) catalysts (black lines) and catalysts frozen under applied catalytic potential after conditioning at 1.63 V_{RHE} for 30 min in 0.1 M KOH (colored lines) measured at the (c) Ni *K*-edge and (d) Fe *K*-edge. The catalyst composition is indicated as atomic % Fe. Fit parameters are listed in Table 1 and Supporting Information S6, Tables S1–S7.

observed in several in situ XAS studies of mixed Ni–Fe catalysts.[18,31,39,47] Conflicting results regarding the Fe oxidation state of our catalysts compared to other studies, where Fe^{+4} has been observed[44,46] up to a molar fraction of ~12 % at similar catalytic potentials,[46] might be attributed to the sensitivity of the respective methods. The presence of Fe^{4+} sites can therefore not be excluded in our study; however, the main fraction is confirmed as Fe^{+3}. Distances fitted from the Fe EXAFS showed that the Fe catalyst could be well represented by O coordinated at 1.98 Å and Fe at 3.07 Å (Table 1 and Figure S15–16); however, the amplitudes of the peaks were lower than expected for a highly crystalline phase, suggesting a high distortion of the oxide motifs around the metal center in accordance with the amorphous XRD nature. The oxidation state of the Fe in our mixed Ni–Fe catalyst based on the Fe–O distances obtained from the EXAFS fitting varied between +3.1–3.4, which is in conflict with Fe in oxidation state 3+ as estimated from the *K*-edge positions (see Figure S17 and Table

DOI: 10.1021/jacs.6b00332
J. Am. Chem. Soc. 2016, 138, 5603–5614

Table 1. Fit Parameters Obtained from EXAFS Ni and Fe *K*-Edges of Selected Catalysts Freeze-Quenched under Applied Catalytic Potential of 1.63 V_{RHE}[a]

Fe *K*-edge at 1.63 V_{RHE}						
$Ni_{100-x}Fe_x$	R(Fe−O)/Å	CN	Ox. state	R(Fe−M)/Å	CN	R_f
Fe	1.98 ± 0.02	5.0 ± 0.9	3.4	3.05 ± 0.02	4.9 ± 1.0	20.1
$Ni_{96}Fe_4$	1.99 ± 0.03	5.8 ± 1.0	3.4	3.11 ± 0.01	3.7 ± 0.3	23.0
				2.88 ± 0.02	2.9 ± 0.3	
$Ni_{91}Fe_9$	2.01 ± 0.01	6.3 ± 0.8	3.1	3.12 ± 0.01	6.7 ± 1.0	15.9
$Ni_{65}Fe_{35}$	2.01 ± 0.01	6.2 ± 0.8	3.1	3.09 ± 0.01	6.5 ± 0.8	14.4
$Ni_{45}Fe_{55}$	2.00 ± 0.01	5.2 ± 0.8	3.2	3.08 ± 0.01	3.7 ± 0.5	17.9
$Ni_{28}Fe_{72}$	1.99 ± 0.01	5.4 ± 0.8	3.4	3.07 ± 0.02	3.5 ± 0.7	19.4
Ni *K*-edge at 1.63 V_{RHE}						
$Ni_{100-x}Fe_x$	R(Ni−O)/Å	CN	Ox. state	R(Ni−M)/Å	CN	R_f
Ni	1.88 ± 0.01	4.9 ± 0.3	3.7	2.82 ± 0.01	6.3 ± 0.2	15.2
$Ni_{96}Fe_4$	1.87 ± 0.02	1.9 ± 0.2	3.7	2.83 ± 0.01	2.0 ± 0.2	24.4
	2.06 ± 0.01	4.1 ± 0.2	2.0	3.07 ± 0.01	4.0 ± 0.2	
$Ni_{91}Fe_9$	2.04 ± 0.01	6.6 ± 0.5	2.0	3.09 ± 0.01	5.4 ± 0.3	15.5
$Ni_{65}Fe_{35}$	2.05 ± 0.01	6.6 ± 0.6	2.1	3.08 ± 0.01	4.9 ± 0.2	16.6
$Ni_{45}Fe_{55}$	2.04 ± 0.01	5.6 ± 0.5	2.1	3.08 ± 0.01	3.3 ± 0.1	24.8
$Ni_{28}Fe_{72}$	2.05 ± 0.01	6.7 ± 0.5	2.0	3.07 ± 0.01	4.4 ± 0.2	23.5

[a]Full fit parameters and errors are given in Tables S2−S7. Parameters were obtained from fitting in the k-range of 2.6−12.5 $Å^{-1}$ for the Fe *K*-edge and 2.6−14 $Å^{-1}$ for the Ni *K*-edge. Error values correspond to a 68% confidence interval. Oxidation states were determined from M−O distances (see Figure S17a for oxidation states from *K*-edge positions). Complete fit parameters are given in Supporting Information S6, Tables S1−S7, structural models used for the Fe and Ni *K*-edges are shown in Figure S20−21, and reference compounds in Figure S22 and in Tables S8−S9.

S1). A possible explanation for this discrepancy is that a fraction of the Fe centers are not coordinately saturated, and thus either appear as tetrahedral coordination, or the presence of O vacancies, which would explain a relatively low coordination number.

At the Ni *K*-edge, the XANES spectra of the as-prepared catalysts showed consistently Ni atoms oxidation state +2 independent of Ni−Fe composition (Figure S14b) also supported by the Ni−O distances (Table 1), whereas the Ni-catalyst frozen under catalytic potentials of 1.63 V showed a distinct Ni *K*-edge shift of +2.7 eV (Figure 4b). This is consistent with Ni atoms in changing from oxidation +2 to +4 (+3.7), in accordance with previous reports of formation of a γ-NiOOH phase under catalytic OER potential.[31,41,49,84] The FT-EXAFS of the as-prepared Ni-catalyst showed a nearly perfect match with the layered α-$Ni(OH)_2$[31,41,45,49,85] and with oxygen coordinated at a distance of 2.04 Å and a Ni−Ni coordination at 3.08 Å in the as-prepared state, which upon application of 1.63 V contracted to a short Ni−O distance at 1.87 Å and Ni−Ni coordination at 2.82 Å (see also Figure S15−S16 for EXAFS fits), confirming that Ni atoms oxidized from $Ni^{2+}(OH)_2$ → Ni^{4+}-oxy(hydroxide) under OER potential. In the $Ni_{96}Fe_4$ catalyst, the potential-induced Ni *K*-edge shift was reduced to a +∼0.8 eV shift (Figure 4b). In the Ni FT-EXAFS, this was observed as two split Ni−O distances at 1.87 and 2.06 Å and two split Ni-M distances at 2.83 and 3.07 Å (Figure 4d, S15d, and S17b,c). This indicates that a fraction of the Ni centers remained in oxidation state +2 under applied catalytic potential at 1.63 V. The respective Fe EXAFS of the $Ni_{96}Fe_4$ at 1.63 V showed two clearly separated Fe-M peaks at 2.88 and 3.11 Å, and a slightly broadened Fe−O peak (Figure 4c, Figure S15c, and S17b,c), which implies that Fe is adapting to the changing Ni lattice without changing its oxidation state. Further addition of Fe resulted in a further decline in the potential-induced Ni *K*-edge shift, which was absent at 9% Fe ($Ni_{91}Fe_9$). This would suggest that Ni atoms remain in oxidation state +2 in the OER-active state in the presence of Fe atoms in mixed Ni−Fe centers. This supports the observation regarding the Faradaic efficiency of O_2 as presented in the DEMS study in Figure 2 above, where a contribution of Ni oxidation in the Ni-catalyst was confirmed, however absent in the mixed Ni−Fe catalysts, which showed low charge contributions and high Faradaic efficiencies of ∼90% (see discussion above). Extracted Ni−O and Ni−M trends vs catalyst composition are shown in Figure S17. Fit parameters are listed in Table 1 and Supporting Information S6, Tables S1−S7.

Our results are conflicting previous XAS studies of mixed Ni−Fe catalysts,[4,31,39,41] however have been partly supported.[18,47] We speculate that external influences such as measurement conditions and/or electrode material might play a more important role than previously thought. Possible charge-transfer interactions between the catalyst and Au were highlighted in MnO_x by Gorlin et al.[86] and were recently correlated to an increase in OER activity and Mn oxidation state by Seitz et al.[87] Yeo et al.[59] have also discussed possible charge transfer interactions between NiO_x and Au based on an significant increase in the OER activity. Doyle et al.[88] showed clear differences in the redox wave of NiOOH when deposited on Au, Pt or GC electrodes. Klaus et al.[48] recently confirmed that Au also enhances the OER activity of Fe atoms. Au has been shown to oxidize already at 1.2 V_{RHE} in alkaline electrolyte,[89] and interactions between the catalyst and electrochemically dissolved Au atoms are therefore plausible however has so far not been thoroughly explored. The impact of external influences as a likely explanation for diverging results regarding the Ni oxidation state during OER catalysis in mixed Ni−Fe oxyhydroxides would require further investigations.

3.4.2. Structural Motifs, Amorphicity and Long-Range Order. The Fourier-transformed EXAFS spectra showed two main peaks at the Fe and Ni *K*-edges, one at shorter distance corresponding to the nearest oxygen ligands, and a second peak at longer distance reflecting the nearest metal ligands of the X-ray absorbing metal ion (Figure 4c,d). The positions of these

DOI: 10.1021/jacs.6b00332
J. Am. Chem. Soc. 2016, 138, 5603−5614

peaks and the lack of major peaks at higher distances suggest that the dominant structural motifs in the catalysts were octahedrally coordinated [MO_6] units where Ni and Fe atoms were extensively connected via μ-O(H) bridges. Addition of Fe resulted in decreased FT amplitudes, which was significant at Fe contents above 35%, suggesting that addition of Fe leads to a distortion of the ligand environment around the metal center, in accordance with the increasing atomic amorphicity suggested by the XRD data. Weaker Ni−Ni peaks were visible at longer distances, which can be well described by backscattering from the corresponding Ni atoms within the oxide layer. The FT-EXAFS spectra show that nearly identical spectral motifs were present at both Ni and Fe *K*-edges for the same Ni:Fe composition, which imply that the Ni and Fe atoms formed well-mixed centers. This contrasts findings of Friebel et al.,[31] where it was proposed that Fe nucleates as a separate phase at Fe contents above 25%. In the present study, no detection of metallic Ni or Fe was confirmed. Surprisingly, the Fe atoms contributed to binuclear Ni−Fe motifs at a coordination distance of 3.09 Å (possibly di(μ-OH) bridging) and a shorter distance of 2.86 Å (possibly di(μ-O) bridging), whereas in the Fe catalyst such long or short Fe−Fe distances were not observed. This suggests that Fe was incorporated to form Ni−Fe bonds also at Fe-contents > 25 at %. An increase of the Fe−M amplitudes at 3.45 Å was clearly visible toward high Fe contents under catalytic OER potentials. This distance indicates the presence of corner-sharing octahedra,[90] which have been proved computationally to be thermodynamically feasible in β-Ni(OH)$_2$.[36] This may also be explained by aggregation of metal-oxo octahedra undergoing condensation during catalysis, where if hydrated oxyhydroxide layers attaching end-by-end would result in such distance,[90] however this has so far non been extensively discussed in terms of mixed Ni−Fe oxyhydroxides. Presented SEM images (Figure S12−S13) are supportive of a rearrangement with visible changes in the morphology during applied OER potential in the mixed $Ni_{45}Fe_{55}$ catalyst.

Catalysts frozen under catalytic OER potential of 1.63 V showed an increase in the FT-EXAFS amplitudes compared to the as-prepared catalysts both at the Ni and Fe *K*-edge clearly revealed in Figure S18 (see also Figure S19 for XANES and EXAFS). We notice that this increase is not caused specifically by the application of catalytic potential since catalysts frozen under non catalytic potential (1.0 V) showed even higher FT-EXAFS amplitudes than catalysts conditioned at 1.63 V. The $Ni_{45}Fe_{55}$ catalyst showing highest OER activity also preserved highest distortion around the metal center in the active state (visible in Figure 4d). Thus, high catalytic OER activity is correlated with higher distortion around the metal center. This would suggest that high activity is associated with a highly disordered state, which could be ascribed to high amorphicity. This could on the other hand be reflected in the number of highly active Ni−Fe centers, and thus would be most visible in the catalyst with a high turnover.

3.5. Correlation of Activity, Faradaic Efficiency, and Metal Redox States. This section establishes a plausible correlation of the voltammetric, XAS, and DEMS results and seeks reconciliation with earlier reports. Key findings of our present study are illustrated in Figure 5. The Ni-catalyst with its edge-connected octahedral structural motifs undergoes a pronounced redox state change between +2 and +3/+4 under OER conditions, evidenced by both XAS and DEMS-based faradaic efficiency data. In presence of Fe, however, data

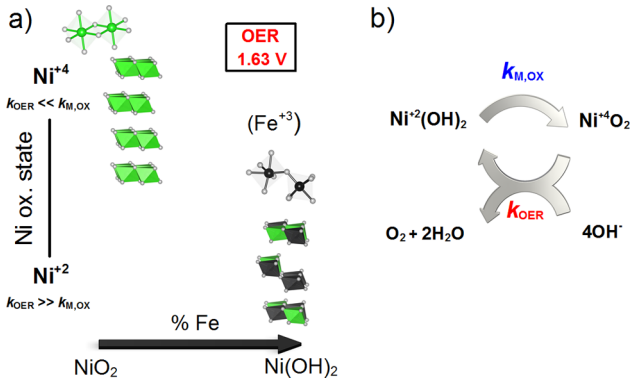

Figure 5. (a) XAS-derived structural motifs prevalent during OER catalysis at high and intermediate Ni-content. At high Ni-content the dominating host is the layered γ-NiOOH (a "NiO_2" phase) with octahedrally coordinated edge-sharing Ni^{4+}. In the presence of Fe there is a mixture of edge- and corner sharing octahedra.[76,90,91] Above 4% Fe, the dominant host is the Ni(OH)$_2$ with Ni^{2+}. (b) Simplified scheme of the electrochemical water splitting cycle with metal oxidation rate constant, $k_{M,OX}$, and the catalytic OER rate constant, k_{OER}.

suggested a stabilization of low-valent Ni centers, in particular for the most active mixed Ni−Fe catalysts. Pure Fe centers essentially showed no change in their redox state, as well. Our XAS results pointed in the same direction given the absence of any potential-induced Ni or Fe *K*-edge shift of the Fe-containing catalysts under catalytic reaction conditions. At the same time, corner-connected Fe−O octahedra emerge as a prominent structural motif. While these results are in agreement with a number of previous studies,[31,44,47] they are partially in conflict with others.[31,46] These conflicting reports on the metal oxidation state bear the question whether the catalytically most active metal centers actually remain in low-valent states, or whether there are other mechanisms or external influences that make the observation of low-valent states under certain experimental and catalytic conditions extremely challenging as discussed above.

Intuitively, one would expect the metal redox centers to build up oxidation equivalents during the catalytic cycles. So, a muted redox activity of the Ni and the suspected active Fe centers appears implausible. A simple argument states that the bulk-sensitive XAS methods may miss the catalytic redox processes near surfaces. However, this can be ruled out based on the fact that the XAS analysis of the pure Ni-catalyst showed indeed strong variations in its redox state. In addition, the DEMS results gave independent evidence for significantly reduced charge injection associated with metal redox processes.

Assuming the muted metal redox processes are real, one may argue that the presence of Fe centers might have shifted the neighboring Ni^{2+} oxidation potential to such positive values that Ni^{2+} oxidation is no longer energetically possible at +1.63 V. The electrochemical data, however, are in conflict with this view. The Ni(OH)$_2$/NiOOH redox peak does indeed shift by ~70 mV from +1.38 V to +1.45 V (see Figure 1) at increasing Fe contents: the midpoint potential, however, is still clearly below the applied potential of +1.63 V. Thus, the population of Ni atoms at catalytic potential should include formation of Ni^{4+}OOH.

An alternative hypothesis to reconcile conflicting results regarding the actual metal redox state under catalytic conditions is outlined in Figure 5b. We represent an individual catalytic

DOI: 10.1021/jacs.6b00332
J. Am. Chem. Soc. 2016, 138, 5603−5614

OER cycle by a very simplified reaction scheme, where the buildup of oxidation equivalents from Ni^{2+} to Ni^{4+} (or Fe^{3+} to Fe^{4+}) sites is followed by the O−O bond formation with the subsequent release of molecular oxygen. This process restores the metal site back to its reduced state. The full cycle thus can be split into two consecutive processes that are assumed to proceed with the reaction rate constants $k_{M,ox}$ and k_{OER}, respectively (see Figure 5b).

It has been shown for various water-oxidizing oxides of monometallic first-row transition metals that the second water-oxidation−metal-reduction step is slower (rate-limiting) than the metal oxidation ($k_{Mox} \gg k_{OER}$) which results in accumulation of high-valent metal species at catalytic potentials. In our bimetallic Ni−Fe catalysts, however, the presence of Fe enhances the OER rate by 1−2 orders of magnitude. This increase reflects a dramatically increased rate constant, k_{OER}, which may exceed the rate of the metal oxidation, i.e., $k_{OER} \gg k_{Mox}$. The origin of the increased OER activity in terms of faster OER rate constant have been discussed previously as a plausible explanation;[28,30] however, evidence of low valent Ni could not be confirmed. Under these conditions, a significant accumulation of high-valent metal centers is prevented, even though the reaction cycle does involve formation of high-valent metal ions.

Our hypothesis reconciles voltammetric, DEMS and XAS data consistently. It predicts that the observation of Ni in its high-valent state critically depends on the $k_{M,ox}/k_{OER}$ ratio. Subtle differences between catalyst materials, or external influences, thus could favor or disfavor detection of Ni^{4+} ions at OER potentials so that our model offers a simple explanation for conflicting results in previous reports.

4. CONCLUSIONS

We have characterized and correlated the OER reaction dynamics, the faradaic charge efficiency, and the corresponding metal redox states of Ni−Fe oxyhydroxide electrocatalysts. To achieve this, we combined operando electrochemical mass spectrometry (DEMS) and X-ray absorption spectroscopy (XAS) with electrochemical characterization. Our results and conclusions offer new fundamental insights into the reaction dynamics and the state of the metal centers under reactive conditions. Our critical discussion of the present results in light of previous reports has resulted in a simple mechanistic model hypothesis that is capable to resolve conflicting past reports on the prevailing active metal redox states.

We investigated amorphous Ni−Fe catalysts with various compositions (0−100 at. % Fe). The highest OER activity was observed around a 50% Fe, supported by low Tafel slopes in the order of 35 mV dec^{-1}. Tracking the evolution of the normalized $Ni^{2+/3+}$ redox charge evidenced that the OER catalysis needs to be recognized as a volume, not as a surface process. The continuous change in the electrochemical properties of the Ni−Fe(OOH) series excludes the formation of separate Ni- and Fe-oxide phases or metallic Ni, instead suggests the formation of a well-mixed bimetallic phase with catalytic properties determined by the Ni:Fe stoichiometry.

The deconvolution of faradaic processes using operando DEMS allowed for relating the evolution of O_2 to the metal redox state changes. For the NiOOH catalyst, there was a large charge contribution process not resulting in product formation and a low faradaic efficiency (max ∼60%), which evidenced the presence of Ni^{4+}. The presence of Fe (while boosting the OER activity) diminished the charge contribution process of Ni^{4+}, reaching faradaic efficiencies in the order of ∼90%.

Quasi-in situ X-ray absorption spectroscopy confirmed the DEMS-based conclusions. They showed that the oxidation state of Ni atoms in the mixed Ni−Fe electrocatalysts under catalytic OER conditions were highly dependent on the Ni:Fe stoichiometry whereas the Fe oxidation state was not. The Fe structure was best described as a highly distorted $Fe^{3+}OOH$ with a mixture of edge-sharing and corner-sharing octahedra. The Ni structure was well described as α-$Ni(OH)_2$ with Ni in oxidation state +2 in the as-prepared state. Under catalytic conditions, Ni atoms were present as Ni^{4+} at Fe content below 4%, and above, Ni atoms were stabilized in low-valent oxidation state under catalytic conditions, and thus the OER active state could be described as $Ni^{2+}Fe^{3+}OOH$. At the Fe *K*-edge, there was no visible *K*-edge shift for any composition; however, a strong Fe-M bond contraction was observed, well correlated with the lattice contraction in the Ni host.

Finally, a simple mechanistic hypothesis was put forward to explain why the experimental detection of Ni centers predominantly in lower-valent states do not preclude an efficient electrocatalytic water splitting process where redox equivalents are accumulated in the metal centers. The mechanistic hypothesis highlights the fact that the detection of metal centers in high-valent states critically depends on the $k_{M,ox}/k_{OER}$ ratio. High catalytic OER activity of the mixed Ni−Fe catalysts sharply decreases this ratio; the population of high-valent Ni atoms are depressed due to a faster OER rate constant in comparison to the metal oxidation step ($k_{OER} \gg k_{M,ox}$). This hypothesis plausibly explains water oxidation at seemingly low-valent metal centers and reconciles past diverging reports.

■ ASSOCIATED CONTENT

Supporting Information

The Supporting Information is available free of charge on the ACS Publications website at DOI: 10.1021/jacs.6b00332.

Experimental details and additional electrochemical and structural characterization. (PDF)

■ AUTHOR INFORMATION

Corresponding Authors

*holger.dau@fu-berlin.de

*pstrasser@tu-berlin.de

Notes

The authors declare no competing financial interest.

■ ACKNOWLEDGMENTS

This project received financial support by the Bundesministerium für Bildung und Forschung (BMBF) under grant 03SF0433A−"MEOKATS". P.S. acknowledges partial funding by the German Federal Ministry of Education and Research (Bundesministerium für Bildung und Forschung, BMBF) under grant #03SF0523A−"CO2EKAT". We thank the Helmholtz-Zentrum Berlin (HZB) for allocation of synchrotron radiation beamtime at KMC-1 and KMC-3 (BESSY synchrotron, Berlin Adlershof), and we gratefully acknowledge support by Marcel Mertin, Dr. Franz Schäfers, and Dr. Ivo Zizak (all BESSY/HZB). This project also received financial support by the Berlin cluster of excellence "UniCat".

DOI: 10.1021/jacs.6b00332
J. Am. Chem. Soc. 2016, 138, 5603−5614

REFERENCES

(1) Nocera, D. G. *Inorg. Chem.* **2009**, *48*, 10001.
(2) Dau, H.; Limberg, C.; Reier, T.; Risch, M.; Roggan, S.; Strasser, P. *ChemCatChem* **2010**, *2*, 724.
(3) Trasatti, S. *J. Electroanal. Chem. Interfacial Electrochem.* **1980**, *111*, 125.
(4) de Levie, R. *J. Electroanal. Chem.* **1999**, *476*, 92.
(5) Walter, M. G.; Warren, E. L.; McKone, J. R.; Boettcher, S. W.; Mi, Q.; Santori, E. A.; Lewis, N. S. *Chem. Rev.* **2010**, *110*, 6446.
(6) Man, I. C.; Su, H. Y.; Calle-Vallejo, F.; Hansen, H. A.; Martinez, J. I.; Inoglu, N. G.; Kitchin, J.; Jaramillo, T. F.; Norskov, J. K.; Rossmeisl, J. *ChemCatChem* **2011**, *3*, 1159.
(7) Subbaraman, R.; Tripkovic, D.; Chang, K. C.; Strmcnik, D.; Paulikas, A. P.; Hirunsit, P.; Chan, M.; Greeley, J.; Stamenkovic, V.; Markovic, N. M. *Nat. Mater.* **2012**, *11*, 550.
(8) Liao, P.; Keith, J. A.; Carter, E. A. *J. Am. Chem. Soc.* **2012**, *134*, 13296.
(9) Singh, A.; Spiccia, L. *Coord. Chem. Rev.* **2013**, *257*, 2607.
(10) McCrory, C. C. L.; Jung, S.; Peters, J. C.; Jaramillo, T. F. *J. Am. Chem. Soc.* **2013**, *135*, 16977.
(11) Hu, S.; Xiang, C.; Haussener, S.; Berger, A. D.; Lewis, N. S. *Energy Environ. Sci.* **2013**, *6*, 2984.
(12) Jin, J.; Walczak, K.; Singh, M. R.; Karp, C.; Lewis, N. S.; Xiang, C. *Energy Environ. Sci.* **2014**, *7*, 3371.
(13) Frydendal, R.; Paoli, E. A.; Knudsen, B. P.; Wickman, B.; Malacrida, P.; Stephens, I. E. L.; Chorkendorff, I. *ChemElectroChem* **2014**, *1*, 2075.
(14) Trotochaud, L.; Mills, T. J.; Boettcher, S. W. *J. Phys. Chem. Lett.* **2013**, *4*, 931.
(15) Burke, M. S.; Kast, M. G.; Trotochaud, L.; Smith, A. M.; Boettcher, S. W. *J. Am. Chem. Soc.* **2015**, *137*, 3638.
(16) Miller, E. L.; Rocheleau, R. E. *J. Electrochem. Soc.* **1997**, *144*, 3072.
(17) Kleiman-Shwarsctein, A.; Hu, Y. S.; Stucky, G. D.; McFarland, E. W. *Electrochem. Commun.* **2009**, *11*, 1150.
(18) Landon, J.; Demeter, E.; Inoglu, N.; Keturakis, C.; Wachs, I. E.; Vasic, R.; Frenkel, A. I.; Kitchin, J. R. *ACS Catal.* **2012**, *2*, 1793.
(19) Trotochaud, L.; Ranney, J. K.; Williams, K. N.; Boettcher, S. W. *J. Am. Chem. Soc.* **2012**, *134*, 17253.
(20) Smith, R. D. L.; Prevot, M. S.; Fagan, R. D.; Trudel, S.; Berlinguette, C. P. *J. Am. Chem. Soc.* **2013**, *135*, 11580.
(21) Gong, M.; Li, Y.; Wang, H.; Liang, Y.; Wu, J. Z.; Zhou, J.; Wang, J.; Regier, T.; Wei, F.; Dai, H. *J. Am. Chem. Soc.* **2013**, *135*, 8452.
(22) Hunter, B. M.; Blakemore, J. D.; Deimund, M.; Gray, H. B.; Winkler, J. R.; Müller, A. M. *J. Am. Chem. Soc.* **2014**, *136*, 13118.
(23) Chen, J. Y. C.; Miller, J. T.; Gerken, J. B.; Stahl, S. S. *Energy Environ. Sci.* **2014**, *7*, 1382.
(24) Oliver-Tolentino, M. A.; Vázquez-Samperio, J.; Manzo-Robledo, A.; González-Huerta, R. d. G.; Flores-Moreno, J. L.; Ramírez-Rosales, D.; Guzmán-Vargas, A. *J. Phys. Chem. C* **2014**, *118*, 22432.
(25) Gong, M.; Dai, H. *Nano Res.* **2015**, *8*, 23.
(26) Feng, Y.; Zhang, H.; Zhang, Y.; Li, X.; Wang, Y. *ACS Appl. Mater. Interfaces* **2015**, *7*, 9203.
(27) Smith, A. M.; Trotochaud, L.; Burke, M. S.; Boettcher, S. W. *Chem. Commun.* **2015**, *51*, 5261.
(28) Trotochaud, L.; Young, S. L.; Ranney, J. K.; Boettcher, S. W. *J. Am. Chem. Soc.* **2014**, *136*, 6744.
(29) Dionigi, F.; Reier, T.; Pawolek, Z.; Gliech, M.; Strasser, P. *ChemSusChem* **2016**, *9*, 1.
(30) Louie, M. W.; Bell, A. T. *J. Am. Chem. Soc.* **2013**, *135*, 12329.
(31) Friebel, D.; Louie, M. W.; Bajdich, M.; Sanwald, K. E.; Cai, Y.; Wise, A. M.; Cheng, M.-J.; Sokaras, D.; Weng, T.-C.; Alonso-Mori, R.; Davis, R. C.; Bargar, J. R.; Nørskov, J. K.; Nilsson, A.; Bell, A. T. *J. Am. Chem. Soc.* **2015**, *137*, 1306.
(32) Hong, D. C.; Yamada, Y.; Nagatomi, T.; Takai, Y.; Fukuzumi, S. *J. Am. Chem. Soc.* **2012**, *134*, 19572.
(33) Wang, L.; Dionigi, F.; Nguyen, N. T.; Kirchgeorg, R.; Gliech, M.; Grigorescu, S.; Strasser, P.; Schmuki, P. *Chem. Mater.* **2015**, *27*, 2360.
(34) Luo, J.; Im, J.-H.; Mayer, M. T.; Schreier, M.; Nazeeruddin, M. K.; Park, N.-G.; Tilley, S. D.; Fan, H. J.; Grätzel, M. *Science* **2014**, *345*, 1593.
(35) Hu, C.-C.; Wu, Y.-R. *Mater. Chem. Phys.* **2003**, *82*, 588.
(36) Qiu, Y.; Xin, L.; Li, W. *Langmuir* **2014**, *30*, 7893.
(37) Yu, X.; Zhang, M.; Yuan, W.; Shi, G. *J. Mater. Chem. A* **2015**, *3*, 6921.
(38) Li, X.; Walsh, F. C.; Pletcher, D. *Phys. Chem. Chem. Phys.* **2011**, *13*, 1162.
(39) Kim, S.; Tryk, D. A.; Antonio, M. R.; Carr, R.; Scherson, D. *J. Phys. Chem.* **1994**, *98*, 10269.
(40) del Arco, M.; Malet, P.; Trujillano, R.; Rives, V. *Chem. Mater.* **1999**, *11*, 624.
(41) Balasubramanian, M.; Melendres, C. A.; Mini, S. *J. Phys. Chem. B* **2000**, *104*, 4300.
(42) Trześniewski, B. J.; Diaz-Morales, O.; Vermaas, D. A.; Longo, A.; Bras, W.; Koper, M. T. M.; Smith, W. A. *J. Am. Chem. Soc.* **2015**, *137*, 15112.
(43) Morales-Guio, C. G.; Mayer, M. T.; Yella, A.; Tilley, S. D.; Grätzel, M.; Hu, X. *J. Am. Chem. Soc.* **2015**, *137*, 9927.
(44) Wang, D.; Zhou, J.; Hu, Y.; Yang, J.; Han, N.; Li, Y.; Sham, T.-K. *J. Phys. Chem. C* **2015**, *119*, 19573.
(45) Ogrady, W. E.; Pandya, K. I.; Swider, K. E.; Corrigan, D. A. *J. Electrochem. Soc.* **1996**, *143*, 1613.
(46) Chen, J. Y. C.; Dang, L.; Liang, H.; Bi, W.; Gerken, J. B.; Jin, S.; Alp, E. E.; Stahl, S. S. *J. Am. Chem. Soc.* **2015**, *137*, 15090.
(47) Bates, M. K.; Jia, Q.; Doan, H.; Liang, W.; Mukerjee, S. *ACS Catal.* **2016**, *6*, 155.
(48) Klaus, S.; Cai, Y.; Louie, M. W.; Trotochaud, L.; Bell, A. T. *J. Phys. Chem. C* **2015**, *119*, 7243.
(49) Risch, M.; Klingan, K.; Heidkamp, J.; Ehrenberg, D.; Chernev, P.; Zaharieva, I.; Dau, H. *Chem. Commun.* **2011**, *47*, 11912.
(50) Zaharieva, I.; Chernev, P.; Risch, M.; Klingan, K.; Kohlhoff, M.; Fischer, A.; Dau, H. *Energy Environ. Sci.* **2012**, *5*, 7081.
(51) Niederberger, M.; Garnweitner, G.; Buha, J.; Polleux, J.; Ba, J. H.; Pinna, N. *J. Sol-Gel Sci. Technol.* **2006**, *40*, 259.
(52) Pinna, N.; Niederberger, M. *Angew. Chem., Int. Ed.* **2008**, *47*, 5292.
(53) Jusys, Z.; Massong, H.; Baltruschat, H. *J. Electrochem. Soc.* **1999**, *146*, 1093.
(54) Wolter, O.; Heitbaum, J. *Berichte der Bunsengesellschaft für physikalische Chemie* **1984**, *88*, 2.
(55) Baltruschat, H. *J. Am. Soc. Mass Spectrom.* **2004**, *15*, 1693.
(56) Barra, M.; Haumann, M.; Loja, P.; Krivanek, R.; Grundmeier, A.; Dau, H. *Biochemistry* **2006**, *45*, 14523.
(57) Ankudinov, A. L.; Ravel, B.; Rehr, J. J.; Conradson, S. D. *Phys. Rev. B: Condens. Matter Mater. Phys.* **1998**, *58*, 7565.
(58) Rehr, J. J.; Albers, R. C. *Rev. Mod. Phys.* **2000**, *72*, 621.
(59) Yeo, B. S.; Bell, A. T. *J. Phys. Chem. C* **2012**, *116*, 8394.
(60) Trotochaud, L.; Boettcher, S. W. *Scr. Mater.* **2014**, *74*, 25.
(61) Fominykh, K.; Chernev, P.; Zaharieva, I.; Sicklinger, J.; Stefanic, G.; Döblinger, M.; Müller, A.; Pokharel, A.; Böcklein, S.; Scheu, C.; Bein, T.; Fattakhova-Rohlfing, D. *ACS Nano* **2015**, *9*, 5180.
(62) Batchellor, A. S.; Boettcher, S. W. *ACS Catal.* **2015**, *5*, 6680.
(63) Görlin, M.; Gliech, M.; Ferreira de Araújo, J.; Dresp, S.; Bergmann, A.; Strasser, P. *Catal. Today* **2015**, *262*, 65.
(64) Lu, X.; Zhao, C. *Nat. Commun.* **2015**, *6*, 6616.
(65) Smith, R. D. L.; Berlinguette, C. P. *J. Am. Chem. Soc.* **2016**, *138*, 1561.
(66) Risch, M.; Ringleb, F.; Kohlhoff, M.; Bogdanoff, P.; Chernev, P.; Zaharieva, I.; Dau, H. *Energy Environ. Sci.* **2015**, *8*, 661.
(67) González-Flores, D.; Sánchez, I.; Zaharieva, I.; Klingan, K.; Heidkamp, J.; Chernev, P.; Menezes, P. W.; Driess, M.; Dau, H.; Montero, M. L. *Angew. Chem., Int. Ed.* **2015**, *54*, 2472.
(68) Iwasaki, T.; Yoshii, H.; Nakamura, H.; Watano, S. *Appl. Clay Sci.* **2012**, *58*, 120.
(69) Kim, M. S.; Hwang, T. S.; Kim, K. B. *J. Electrochem. Soc.* **1997**, *144*, 1537.

DOI: 10.1021/jacs.6b00332
J. Am. Chem. Soc. 2016, 138, 5603−5614

(70) Wehrens-Dijksma, M.; Notten, P. H. L. *Electrochim. Acta* **2006**, *51*, 3609.
(71) Shangguan, E.; Tang, H.; Chang, Z.; Yuan, X.-Z.; Wang, H. *Int. J. Hydrogen Energy* **2011**, *36*, 10057.
(72) Stern, L.-A.; Hu, X. *Faraday Discuss.* **2014**, *176*, 363.
(73) Hall, D. S.; Lockwood, D. J.; Bock, C.; MacDougall, B. R. *Proc. R. Soc. London, Ser. A* **2015**, *471*, 1.
(74) Eggleton, R. A.; Fitzpatrick, R. W. *Clays Clay Miner.* **1988**, *36*, 111.
(75) Michel, F. M.; Ehm, L.; Antao, S. M.; Lee, P. L.; Chupas, P. J.; Liu, G.; Strongin, D. R.; Schoonen, M. A. A.; Phillips, B. L.; Parise, J. B. *Science* **2007**, *316*, 1726.
(76) Manceau, A. *Clay Miner.* **2009**, *44*, 19.
(77) Michel, F. M.; Barrón, V.; Torrent, J.; Morales, M. P.; Serna, C. J.; Boily, J.-F.; Liu, Q.; Ambrosini, A.; Cismasu, A. C.; Brown, G. E. *Proc. Natl. Acad. Sci. U. S. A.* **2010**, *107*, 2787.
(78) Das, S.; Hendry, M. J.; Essilfie-Dughan, J. *Environ. Sci. Technol.* **2011**, *45*, 268.
(79) Gilbert, B.; Erbs, J. J.; Penn, R. L.; Petkov, V.; Spagnoli, D.; Waychunas, G. A. *Am. Mineral.* **2013**, *98*, 1465.
(80) Mansour, S. A. A. *Thermochim. Acta* **1993**, *228*, 173.
(81) Rives, V.; Angeles Ulibarri, M. a. *Coord. Chem. Rev.* **1999**, *181*, 61.
(82) Wang, K.; He, X.; Li, X.; Jiang, J.; Sun, Y. *Rare Met.* **2009**, *28*, 500.
(83) Bergmann, A.; Martinez-Moreno, E.; Teschner, D.; Chernev, P.; Gliech, M.; de Araujo, J. F.; Reier, T.; Dau, H.; Strasser, P. *Nat. Commun.* **2015**, *6*, 1.
(84) Capehart, T. W.; Corrigan, D. A.; Conell, R. S.; Pandya, K. I.; Hoffman, R. W. *Appl. Phys. Lett.* **1991**, *58*, 865.
(85) Pandya, K. I.; Ogrady, W. E.; Corrigan, D. A.; McBreen, J.; Hoffman, R. W. *J. Phys. Chem.* **1990**, *94*, 21.
(86) Gorlin, Y.; Chung, C.-J.; Benck, J. D.; Nordlund, D.; Seitz, L.; Weng, T.-C.; Sokaras, D.; Clemens, B. M.; Jaramillo, T. F. *J. Am. Chem. Soc.* **2014**, *136*, 4920.
(87) Seitz, L. C.; Hersbach, T. J. P.; Nordlund, D.; Jaramillo, T. F. *J. Phys. Chem. Lett.* **2015**, *6*, 4178.
(88) Doyle, R. L.; Godwin, I. J.; Brandon, M. P.; Lyons, M. E. G. *Phys. Chem. Chem. Phys.* **2013**, *15*, 13737.
(89) Cherevko, S.; Zeradjanin, A. R.; Keeley, G. P.; Mayrhofer, K. J. J. *J. Electrochem. Soc.* **2014**, *161*, H822.
(90) Jolivet, J.-P.; Tronc, E.; Chanéac, C. *C. R. Geosci.* **2006**, *338*, 488.
(91) Sadeghi, O.; Zakharov, L. N.; Nyman, M. *Science* **2015**, *347*, 1359.

DOI: 10.1021/jacs.6b00332
J. Am. Chem. Soc. 2016, 138, 5603−5614